

ORIGINAL ARTICLE

Performance of dual-channel codeless and semicodeless processing

John W. Betz  | Alessandro P. Cerruti 

The MITRE Corporation Bedford,
Massachusetts

Correspondence

The MITRE Corporation, 202 Burlington
Rd., Bedford, MA 01730.
Email: betz@mitre.org

Funding information

U.S. Air Force, Grant/Award Number:
Contract No FA8702-19-C-0001

Abstract

While dual-channel codeless and semicodeless processing are mature techniques used on the Global Positioning System P(Y) signals, the literature lacks assessment of their performance, with derivations from first principles. This paper fills that gap, providing mathematical models of three dual-channel codeless or semicodeless processing approaches. Each exploits a situation where the same signal is transmitted on two carrier frequencies, and the receiver cannot generate a signal replica for conventional processing. The mathematical formulation leads to derivation of analytical models for performance of the three techniques, all having the same parametric form but different parameter values. The models apply to more general cases than previously addressed, allowing any relationship between input signal-to-noise ratios, and including different signal design variants. Computer simulations crosscheck the analytical performance, and comprehensive numerical results are provided. The results provide the foundation for a companion paper assessing how GPS III signal generation affects these types of receivers.

1 | INTRODUCTION

For many years, dual-channel codeless and semicodeless processing of the GPS P(Y) signals on the L1 and L2 carrier frequencies has been performed.¹⁻⁴ This processing enables civil receivers to perform highly accurate dual-frequency carrier phase tracking without accessing a GPS civil signal on a second frequency. Different approaches have been employed over the years:

- Single-channel codeless processing that exploits the signal's cyclostationarity;
- Dual-channel codeless processing intended to exploit broadcast of identical signals on both carriers;
- Dual-channel semicodeless processing intended to also exploit signal construction involving the product of a higher rate known spreading waveform and an unknown spreading waveform at a known lower chip

rate, producing a higher signal-to-noise ratio estimate of the unknown spreading waveform;

- Dual-channel soft-decision semicodeless processing intended also to exploit the known spreading modulation with unknown spreading code bits, to produce a soft-decision estimate of the unknown spreading waveform.

These different approaches involve progressively more detailed hypotheses about the signal structure and more complex receiver processing.

The classic paper⁴ describes these different approaches and provides some analytical expressions for performance, but without derivation, reference, or justification. That paper focuses specifically on the P(Y) signal, and performance results are tied to the relative P(Y) signal powers on the GPS Block II satellites, with L2 P(Y) power 3 dB less than L1 P(Y) power.

In contrast, this paper addresses dual-frequency processing techniques more generally, providing a unifying framework that includes the three types of dual-channel processing summarized above. It applies to a general class of signal design by allowing the unknown spreading waveform chip rate to be any integer submultiple of the known spreading waveform rate. The resulting performance expressions apply for any relative power between the signals on both channels. Performance is upper bounded by a bilinear function of the two input carrier power to noise power spectral densities. Computer simulations crosscheck the analytical calculations of performance.

Even though the types of processing evaluated in this paper are becoming less used due to the availability of open dual frequency signals, receivers employing this processing are still in use. A companion paper to be published uses the results in this paper to show that a new signal combining technique, employed on GPS Block III satellites, is compatible with these receivers.

The following section describes the signal model employed in this paper, upon which dual-channel codeless and semicodeless processing are based. The subsequent section provides a detailed mathematical description of the three different types of processing considered in this paper, with derivation of the signal and noise characteristics at different points in the processing chain. The casual reader need only examine the block diagrams showing the processing flows, while someone wishing to replicate or extend the analysis will benefit from the mathematical details. The next section then uses the analytical results to develop simple equations that describe processing performance; these expressions should be widely useful. Next, a detailed description is provided for the computer simulation used to corroborate the analytical results. The following section provides performance results for the three different types of processing, showing good correspondence between the analytical expressions and the results from the computer simulation. The last section summarizes this paper. Appendix A provides an example correlation function derivation, while tabulations of numerical results are provided in Appendix B.

2 | SIGNAL MODEL

Hypothesize that $y(t)$ is a baseband direct sequence spread spectrum (DSSS) signal whose spreading modulation is binary phase shift keyed with rectangular spreading symbols (BPSK-R) having the form

$$y(t) = \sum_{k=-\infty}^{\infty} a_k g_{NT_c}(t - kNT_c) \sum_{m=-\infty}^{\infty} b_m g_{T_c}(t - mT_c) \quad (1)$$

$$\sum_{j=-\infty}^{\infty} d_j g_{DT_c}(t - jDT_c)$$

where N is a positive integer, and D is another positive integer much greater than N . Furthermore,

$$g_{\Delta}(t) = \text{rect}_{\Delta}(t) = \begin{cases} 1, & -\Delta/2 \leq t < \Delta/2 \\ 0, & \text{elsewhere} \end{cases} \quad (2)$$

is a rectangle function. The values of T_c , N , and D are known. The chip values $\{b_m\}$ of the higher rate spreading waveform are known, but the chip values $\{a_k\}$ of the other spreading waveform (at the same rate if $N = 1$ or lower rate if $N > 1$) are unknown, as are the data message bits $\{d_j\}$. While this paper is based on BPSK-R spreading modulations, it can readily be extended to other biphasic spreading modulations.

The dual-channel processing examined in this paper is designed to exploit two received baseband waveforms (in practice obtained from two different carrier frequencies denoted L1 and L2)

$$\begin{aligned} r_1(t) &= \alpha_1 y(t + \Delta) e^{i\theta_1(t)} + w_1(t + \Delta) \\ r_2(t) &= \alpha_2 y(t) e^{i\theta_2(t)} + w_2(t) \end{aligned} \quad (3)$$

that each contains the same signal, with $w_1(t)$ and $w_2(t)$ being mutually uncorrelated white noise. Here, the signal in $r_1(t)$ is time shifted by Δ relative to the signal in $r_2(t)$, due to dispersive effects of the ionosphere. The waveforms in Equation (3) are assumed to have been frequency downconverted, and the phase terms $\theta_1(t)$ and $\theta_2(t)$ are assumed to vary slowly. The autocorrelation function (ACF) of the unit power signal is denoted $\bar{R}_y(\tau)$ with power spectral density (PSD) $\bar{\Phi}_y(f) = F\{\bar{R}_y(\tau)\}$ where $F\{\cdot\}$ indicates the Fourier transform. (Since the signal is cyclostationary, its stationarized statistics are used where appropriate in this paper.) All random quantities are modeled as ergodic, and the terminology “unit-power” means the ACF evaluated at zero lag and the corresponding area under the PSD are both unity.

For the BPSK-R signal with chip rate f_c examined in this paper, the unit-power ACF is

$$\bar{R}_y(\tau) = \text{tri}_{1/f_c}(\tau) \quad (4)$$

where

$$\text{tri}_T(\tau) = \begin{cases} 1 - |\tau|/T, & |\tau| \leq T \\ 0, & \text{elsewhere} \end{cases} \quad (5)$$

and the unit-power PSD is

$$\bar{\Phi}_y(f) = \frac{1}{f_c} \text{sinc}^2(\pi f/f_c) \quad (6)$$

where

$$\text{sinc}(x) = \sin(x)/x. \quad (7)$$

The processing estimates and tracks the slowly varying phase $\theta_2(t)$ of the signal on the L2 carrier. In Equation (3), and without loss of generality, $w_1(t)$ and $w_2(t)$ have the same PSD N_0 , but the received signal powers α_1^2 and α_2^2 may differ, with received signal powers defined over a specific bandwidth consistent with signal specifications. Thus, over that specific bandwidth, the ratio of received signal power to noise PSD in the first waveform is

$$(C/N_0)_1 = \alpha_1^2/N_0 \quad (8)$$

while in the second waveform it is

$$(C/N_0)_2 = \alpha_2^2/N_0. \quad (9)$$

3 | PROCESSING MODELS

This section introduces processing models for dual-channel codeless processing, dual-channel semicodeless processing, and dual-channel soft-decision semicodeless processing. All three types of processing follow the same type of flow, with differences only in the processing of $r_1(t)$.

3.1 | General model for dual-channel processing

Figure 1 shows the flow for dual-channel processing, which uses waveforms on any two carrier frequencies,

denoted $r_1(t)$ on L1 and $r_2(t)$ on L2. Both the L1 and L2 received waveforms are bandlimited, nominally to the first nulls of the signal's PSD. The L1 waveform is carrier phase rotated to place the biphasic signal in-phase, then delayed to match the ionospheric delay of the signal on L2. The sources of information for phase rotation and delay are beyond the scope of this paper; for P(Y) signal processing, the published techniques employ tracking the C/A signal to provide the L1 carrier phase. The next step in processing the L1 waveform involves enhancing the signal relative to the noise. Different types of dual-channel processing exploit different levels of hypotheses about the signal structure to perform different types of signal enhancement, as discussed in subsequent sections, resulting in enhanced estimates of part or all the signal. This enhanced L1 signal and remaining noise then multiply the L2 signal plus noise, yielding residual parts of the L2 signal plus noise. Depending upon the specific processing, all or part of the signal may be wiped off, leaving the L2 carrier phase and, in some cases, residual parts of the signal that were not wiped off, with additive noise. Tracking loops are then used to track and wipe off any other parts of the signal that had not been wiped, and then track the L2 carrier phase.

The different dual-channel processing approaches described in subsequent subsections all follow this processing flow, using different techniques for signal enhancement in processing the L1 waveform, leaving different residual signal plus noise after multiplication with the L2 waveform, and needing different tracking loops. In all cases, the tracking loops produce estimates of the L2 signal's carrier phase. However, the inputs to the tracking loops are different in each case, as described in subsequent sections.

The waveforms at Point A and Point B in Figure 1 are common to the processing approaches addressed in this paper, and are defined here. The L1 waveform

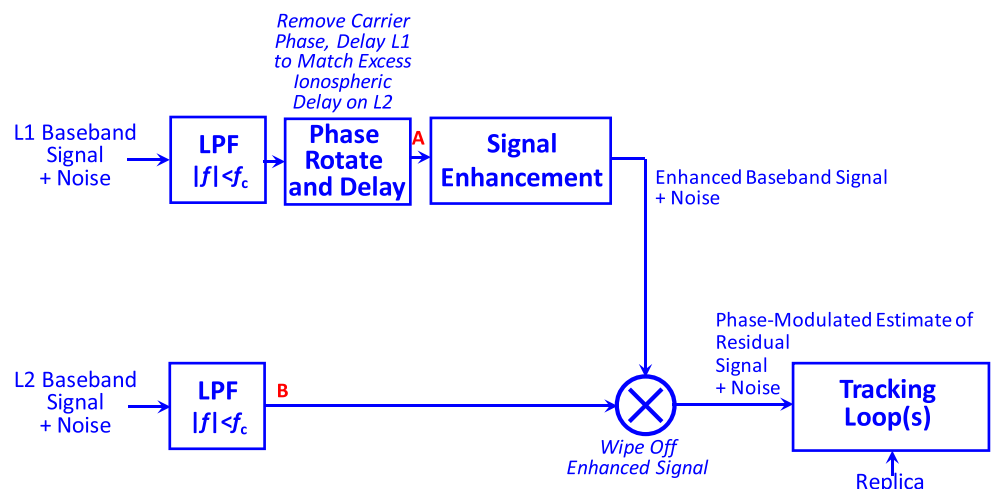


FIGURE 1 General model for dual-channel processing [Color figure can be viewed at wileyonlinelibrary.com and www.ion.org]

after lowpass filtering, phase rotation, and delay is modeled as

$$r_A(t) = [r_1(t)]_{\pm f_c} \cong \phi \alpha_1 y(t) + w_A(t) \quad (10)$$

where $[x(t)]_{\pm \beta}$ indicates bandlimiting $x(t)$ to frequencies $-\beta < f < \beta$, $w_A(t) = [w_1(t)]_{\pm f_c}$, ϕ^2 is the fraction of received signal power passed by the lowpass filtering, and the output signal is approximated as the input signal with reduced amplitude due to lowpass filtering.

Typically, received signal power is defined over a finite signal dual-sided bandwidth, denoted β_T . If the receiver bandlimits to dual-sided bandwidth β_R , then for a signal whose PSD is that of a BPSK-R spreading modulation with spreading code chip rate f_c ,

$$\phi = \left[\frac{\int_{-\beta_R/2}^{\beta_R/2} \text{sinc}^2(\pi f/f_c) df}{\int_{-\beta_T/2}^{\beta_T/2} \text{sinc}^2(\pi f/f_c) df} \right]^{1/2} \quad (11)$$

Observe that as the receiver's lowpass filter bandwidth approaches the transmit bandwidth, ϕ approaches unity. For GPS L1 and L2 P(Y) signals, the dual-sided transmit bandwidth is 30.69 MHz. If the dual-sided lowpass filter bandwidth is 20.46 MHz, $\phi = 0.9847$.

Also,

$$r_B(t) = [r_2(t)]_{\pm f_c} \cong \phi \alpha_2 y(t) e^{i\theta_2(t)} + w_B(t) \quad (12)$$

where $w_B(t) = [w_2(t)]_{\pm f_c}$. The bandlimited noises have the same PSD

$$\Phi_{w_A}(f) = \Phi_{w_B}(f) = N_0 \text{rect}_{2f_c}(f) \quad (13)$$

and ACF

$$R_{w_A}(\tau) = R_{w_B}(\tau) = 2f_c N_0 \text{sinc}(2\pi f_c \tau). \quad (14)$$

The power in the noises at Point A and Point B is $2f_c N_0$.

3.2 | Model for dual-channel codeless processing

Of the dual-channel processing approaches considered in this paper, dual-channel codeless processing, shown in Figure 2, is the simplest. Here, the signal is simply modeled as a biphasic signal, with no other knowledge about its structure. Signal enhancement involves taking the real part of $r_A(t)$, exploiting the L1 biphasic signal that has been phase rotated into the inphase component. Thus, the waveform at Point D is given by (where the "c" in the subscript denotes codeless processing)

$$r_{D,c}(t) = \Re\{r_A(t)\} \cong \phi \alpha_1 y(t) + w_{D,c}(t) \quad (15)$$

where $w_{D,c}(t) = \Re\{[w_1(t)]_{\pm f_c}\}$, which has PSD

$$\Phi_{w_{D,c}}(f) = \frac{N_0}{2} \text{rect}_{2f_c}(f) \quad (16)$$

and ACF

$$R_{w_{D,c}}(\tau) = f_c N_0 \text{sinc}(2\pi f_c \tau) \quad (17)$$

with power $f_c N_0$. Thus, the enhancement processing in this case leaves the signal approximately untouched (neglecting effects of bandlimiting except for the reduction in

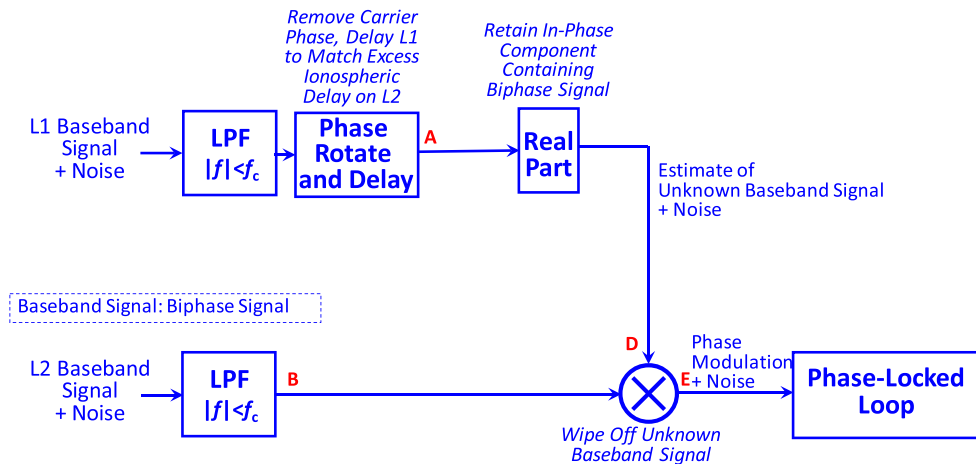


FIGURE 2 Model of dual-channel codeless processing [Color figure can be viewed at wileyonlinelibrary.com and www.ion.org]

power) and reduces the noise power by 3 dB by discarding the part of the noise in phase quadrature to the signal. This architecture is similar to what is called “L1 × L2 Cross-Correlation” in Woo,⁴ although apparently the architecture in Woo⁴ does not exploit the known L1 carrier phase by taking the real part to increase the C/N_0 by 3 dB.

For this dual-channel codeless processing that only exploits the fact that the signal is biphasic, the waveform at Point E is then

$$\begin{aligned}
 r_{E,c}(t) &= r_{D,c}(t)r_B(t) \cong [\phi \alpha_1 y(t) + w_{D,c}(t)] \\
 &\quad \left[\phi \alpha_2 y(t)e^{i\theta_2(t)} + w_B(t) \right] = \phi^2 \alpha_1 \alpha_2 e^{i\theta_2(t)} \\
 &\quad + \phi \alpha_1 y(t)w_B(t) + \phi \alpha_2 y(t)e^{i\theta_2(t)}w_{D,c}(t) \\
 &\quad + w_B(t)w_{D,c}(t).
 \end{aligned} \quad (18)$$

Thus, $r_{E,c}(t)$ takes on the form of a slowly varying complex sinusoid having power

$$(\phi^2 \alpha_1 \alpha_2)^2 = (N_0)^2 \phi^4 (C/N_0)_1 (C/N_0)_2 \quad (19)$$

plus noise $w_{E,c}(t) = w_{E,c,1}(t) + w_{E,c,2}(t) + w_{E,c,3}(t)$, where $w_{E,c,1}(t) = \phi \alpha_1 y(t)w_B(t)$, $w_{E,c,2}(t) = \phi \alpha_2 y(t)e^{i\theta_2(t)}w_{D,c}(t)$, and $w_{E,c,3}(t) = w_B(t)w_{D,c}(t)$.

Thus, a phase-locked loop is used to track the phase of this slowly varying complex sinusoid.

The ACFs of each of the noise terms are approximated by

$$\begin{aligned}
 R_{w_{E,c,1}}(\tau) &\cong 2f_c N_0 \phi^2 \alpha_1^2 \bar{R}_y(\tau) \text{sinc}(2\pi f_c \tau) \\
 &= (N_0)^2 (C/N_0)_1 (2f_c \phi^2) \text{tri}_{1/f_c}(\tau) \text{sinc}(2\pi f_c \tau).
 \end{aligned} \quad (20)$$

$$\begin{aligned}
 R_{w_{E,c,2}}(\tau) &\cong f_c N_0 \phi^2 \alpha_2^2 \bar{R}_y(\tau) \text{sinc}(2\pi f_c \tau) \\
 &= (N_0)^2 (C/N_0)_2 (f_c \phi^2) \text{tri}_{1/f_c}(\tau) \text{sinc}(2\pi f_c \tau).
 \end{aligned} \quad (21)$$

$$R_{w_{E,c,3}}(\tau) \cong (N_0)^2 f_c^2 \text{sinc}^2(2\pi f_c \tau). \quad (22)$$

Appendix A provides an example of the above derivations for Equation (20).

These ACFs and the corresponding PSDs can be computed numerically: $\Phi_{w_{E,c,1}}(f) = F\{R_{w_{E,c,1}}(\tau)\}$, $\Phi_{w_{E,c,2}}(f) = F\{R_{w_{E,c,2}}(\tau)\}$, $\Phi_{w_{E,c,3}}(f) = F\{R_{w_{E,c,3}}(\tau)\}$. The total noise PSD is

$$\Phi_{w_{E,c}}(f) = \Phi_{w_{E,c,1}}(f) + \Phi_{w_{E,c,2}}(f) + \Phi_{w_{E,c,3}}(f). \quad (23)$$

Figure 3 compares the shapes of unit power PSDs numerically computed from Fourier transforms of Equations (20), (21), and (22).

3.3 | Model for dual-channel semicodeless processing

Dual-channel semicodeless processing, shown in Figure 4, is based on modeling the signal structure as the product of a higher rate known spreading waveform and a lower rate spreading waveform with unknown spreading code—hence the term “semicodeless” since one of two spreading codes is known. There, the signal

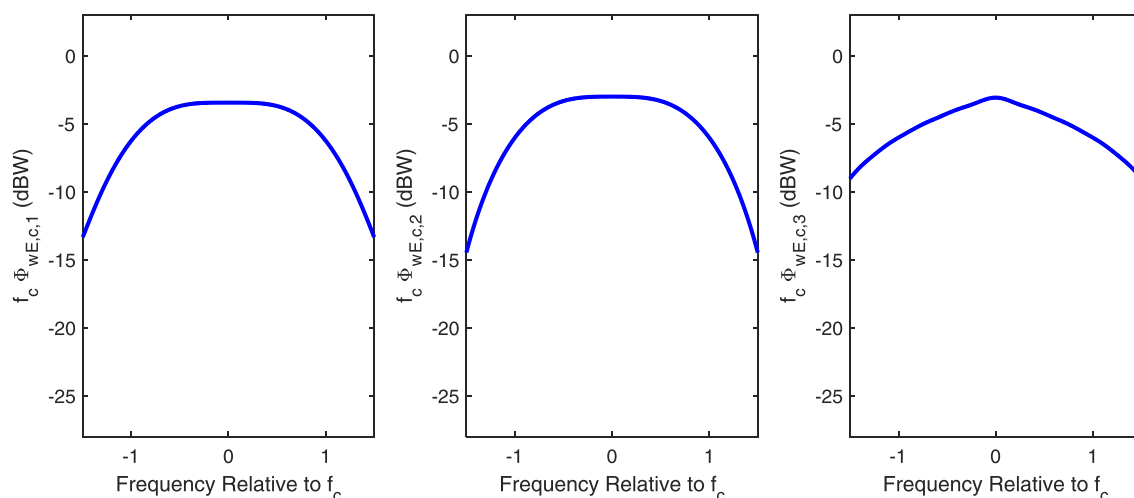


FIGURE 3 Unit-power PSDs for noise terms in dual-channel codeless processing [Color figure can be viewed at wileyonlinelibrary.com and www.ion.org]

enhancement processing in Figure 1 consists of wiping off the higher rate known spreading waveform to reduce the signal bandwidth to that of the lower rate spreading waveform, taking the real part to eliminate noise in phase quadrature to the signal, and lowpass filtering to remove noise outside the reduced signal bandwidth. Removal of L1 delay to match excess ionospheric delay on L2 is an implementation detail not addressed, but assumed to be performed perfectly. This architecture is similar to “P-Code Aided Cross-Correlation” in Woo.⁴

Since the known spreading waveform is synchronized to the signal in $r_A(t)$, the waveform at Point C is

$$\begin{aligned} r_C(t) &= r_A(t) \sum_{m=-\infty}^{\infty} b_m g_{T_c}(t - mT_c) \\ &= \phi \alpha_1 \sum_{k=-\infty}^{\infty} a_k g_{NT_c}(t - kNT_c) \\ &\quad \sum_{j=-\infty}^{\infty} d_j g_{DT_c}(t - jDT_c) + w_C(t) \end{aligned} \quad (24)$$

where $w_C(t) = \Re \left\{ w_A(t) \sum_{m=-\infty}^{\infty} b_m g_{T_c}(t - mT_c) \right\}$. This is a

BPSK-R signal having chip rate f_c/N , with additive noise $w_C(t)$ having ACF

$$R_{w_C}(\tau) = \bar{R}_y(\tau) R_{w_A}(\tau) / 2 = f_c N_0 \text{sinc}(2\pi f_c \tau) \bar{R}_y(\tau) \quad (25)$$

where the division by two comes from taking the real part, reducing the noise power by a factor of two.

The final step in signal enhancement for dual-channel semicodeless processing (indicated by the “s” in the subscript) involves the lowpass filtering, forming

$$\begin{aligned} r_{D,s}(t) &= \lfloor r_C(t) \rfloor_{\pm f_c/N} \cong \phi \alpha_1 \sum_{k=-\infty}^{\infty} a_k g_{NT_c}(t - kNT_c) \\ &\quad \sum_{j=-\infty}^{\infty} d_j g_{DT_c}(t - jDT_c) + w_{D,s}(t) \end{aligned} \quad (26)$$

where $w_{D,s}(t) = \lfloor w_C(t) \rfloor_{\pm f_c/N}$. The lowpass filtering reduces the bandwidth of the noise by a factor of N . Hence, from Equation (25), the power in $w_{D,s}(t)$ is $f_c N_0 / N$.

The approximation in Equation (26) models the signal term as being unchanged from Equation (24), since it is mostly contained in the frequency band $-f_c/N < f < f_c/N$. The ACF of the signal term in $r_{D,s}(t)$ is then approximately

$$0.9028 \phi^2 \alpha_1^2 \text{tri}_{N/f_c}(\tau) \quad (27)$$

where 0.9028 represents the fraction of signal power passed by the null-to-null bandlimiting when N is large. The final multiplication in Figure 4 then wipes off the estimated unknown spreading waveform and the data modulation, leaving the waveform at Point E

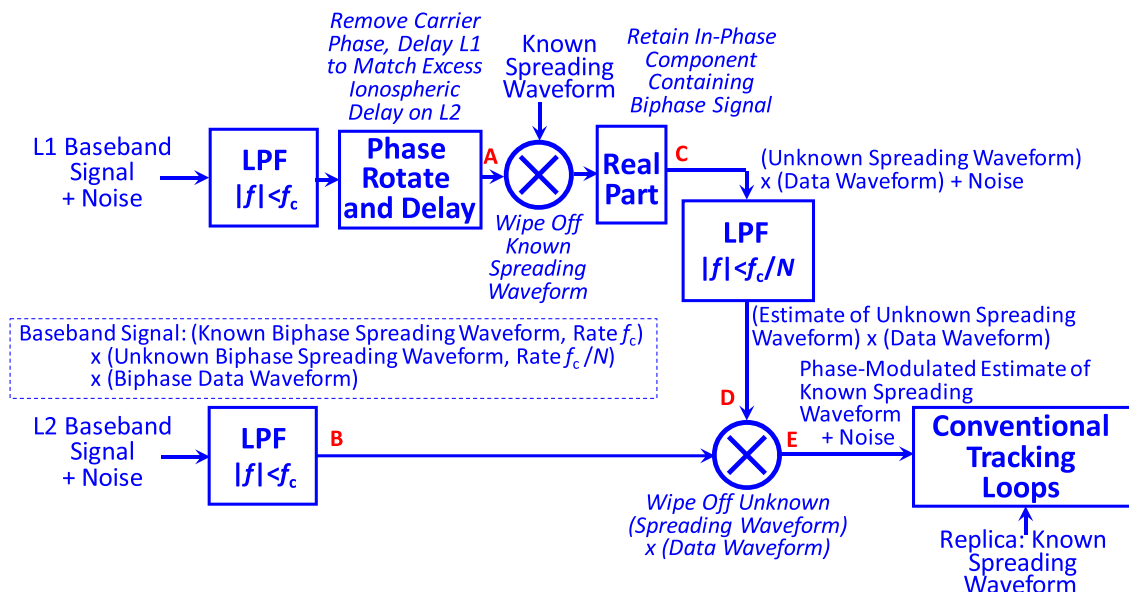


FIGURE 4 Model of dual-channel semicodeless processing [Color figure can be viewed at wileyonlinelibrary.com and www.ion.org]

$$\begin{aligned}
r_{E,s}(t) &= r_B(t)r_{D,s}(t) \cong \left[\sqrt{0.9028} \phi \alpha_1 \sum_{k=-\infty}^{\infty} a_k g_{NT_c}(t-kNT_c) \sum_{j=-\infty}^{\infty} d_j g_{DT_c}(t-jDT_c) + w_{D,s}(t) \right] \\
&\times \left[\phi \alpha_2 \sum_{k=-\infty}^{\infty} a_k g_{NT_c}(t-kNT_c) \sum_{m=-\infty}^{\infty} b_m g_{T_c}(t-mT_c) \sum_{j=-\infty}^{\infty} d_j g_{DT_c}(t-jDT_c) e^{i\theta_2(t)} + w_B(t) \right] \\
&= 0.9502 \phi^2 \alpha_1 \alpha_2 \sum_{m=-\infty}^{\infty} b_m g_{T_c}(t-mT_c) e^{i\theta_2(t)} + w_B(t) \left[0.9502 \phi \alpha_1 \sum_{k=-\infty}^{\infty} a_k g_{NT_c}(t-kNT_c) \sum_{j=-\infty}^{\infty} d_j g_{DT_c}(t-jDT_c) \right] \\
&+ \left[\phi \alpha_2 \sum_{k=-\infty}^{\infty} a_k g_{NT_c}(t-kNT_c) \sum_{m=-\infty}^{\infty} b_m g_{T_c}(t-mT_c) \sum_{j=-\infty}^{\infty} d_j g_{DT_c}(t-jDT_c) e^{i\theta_2(t)} \right] w_{D,s}(t) + w_B(t) w_{D,s}(t). \quad (28)
\end{aligned}$$

This result leads to the conventional process of tracking the carrier phase of a known BPSK-R signal in additive noise.

The conventional tracking loops after Point E wipe off $\sum_{m=-\infty}^{\infty} b_m g_{T_c}(t-mT_c)$ from $r_{E,s}(t)$. The waveform at this Point F is

$$\begin{aligned}
r_{F,s}(t) &= r_{E,s}(t) \sum_{m=-\infty}^{\infty} b_m g_{T_c}(t-mT_c) \cong 0.9502 \quad (29) \\
&\phi^2 \alpha_1 \alpha_2 e^{i\theta_2(t)} + w_{F,s,1}(t) + w_{F,s,2}(t) \\
&+ w_{F,s,3}(t)
\end{aligned}$$

where

$$\begin{aligned}
w_{F,s,1}(t) &\cong w_B(t) \left[\sqrt{0.9028} \phi \alpha_1 \sum_{k=-\infty}^{\infty} a_k g_{NT_c}(t-kNT_c) \right. \\
&\left. \sum_{m=-\infty}^{\infty} b_m g_{T_c}(t-mT_c) \sum_{j=-\infty}^{\infty} d_j g_{DT_c}(t-jDT_c) \right], \\
w_{F,s,2}(t) &\cong \left[\phi \alpha_2 \sum_{k=-\infty}^{\infty} a_k g_{NT_c}(t-kNT_c), \right. \\
&\left. \sum_{j=-\infty}^{\infty} d_j g_{DT_c}(t-jDT_c) e^{i\theta_2(t)} \right] w_{D,s}(t) \\
w_{F,s,3}(t) &\cong w_B(t) w_{D,s}(t) \sum_{m=-\infty}^{\infty} b_m g_{T_c}(t-mT_c).
\end{aligned}$$

The first term in Equation (29) is a slowly varying complex sinusoid having power

$$0.9028 (\phi^2 \alpha_1 \alpha_2)^2 = 0.9028 (N_0)^2 \phi^4 (C/N_0)_1 (C/N_0)_2 \quad (30)$$

summed with three mutually uncorrelated zero-mean noise terms having respective approximate ACFs

$$\begin{aligned}
R_{w_{F,s,1}}(\tau) &\cong 0.9028 \phi^2 \alpha_1^2 \text{tri}_{1/f_c}(\tau) R_{w_B}(\tau) \quad (31) \\
&= 1.8056 \phi^2 (C/N_0)_1 f_c (N_0)^2 \text{tri}_{1/f_c}(\tau) \\
&\quad \text{sinc}(2\pi f_c \tau)
\end{aligned}$$

$$\begin{aligned}
R_{w_{F,s,2}}(\tau) &\cong \phi^2 \alpha_2^2 \text{tri}_{N/f_c}(\tau) R_{w_{D,s}}(\tau) \quad (32) \\
&= \phi^2 (C/N_0)_2 (f_c/N) (N_0)^2 \text{tri}_{N/f_c}(\tau) \\
&\quad \text{sinc}(2\pi f_c \tau/N)
\end{aligned}$$

$$\begin{aligned}
R_{w_{F,s,3}}(\tau) &= R_{w_B}(\tau) R_{w_{D,s}}(\tau) \bar{R}_y(\tau) \cong (f_c N_0)^2 (2/N) \quad (33) \\
&\quad \text{sinc}(2\pi f_c \tau) \text{sinc}(2\pi f_c \tau/N) \text{tri}_{1/f_c}(\tau).
\end{aligned}$$

These ACFs and the corresponding PSDs can be computed numerically: $\Phi_{w_{F,s,1}}(f) = F\{R_{w_{F,s,1}}(\tau)\}$, $\Phi_{w_{F,s,2}}(f) = F\{R_{w_{F,s,2}}(\tau)\}$, and $\Phi_{w_{F,s,3}}(f) = F\{R_{w_{F,s,3}}(\tau)\}$. Figure 5 compares the shapes of unit power PSDs numerically computed from Fourier transforms of Equations (31), (32), and (33). Clearly, $w_{F,s,2}(t)$ has much narrower bandwidth than the other noise terms, concentrating its power in band center.

3.4 | Model for dual-channel soft-decision semicodeless processing

Dual-channel soft-decision semicodeless processing, shown in Figure 6, is equivalent to Z-tracking in Woo.⁴ It is based on assuming even more detail about the signal structure—the known spreading modulation—and

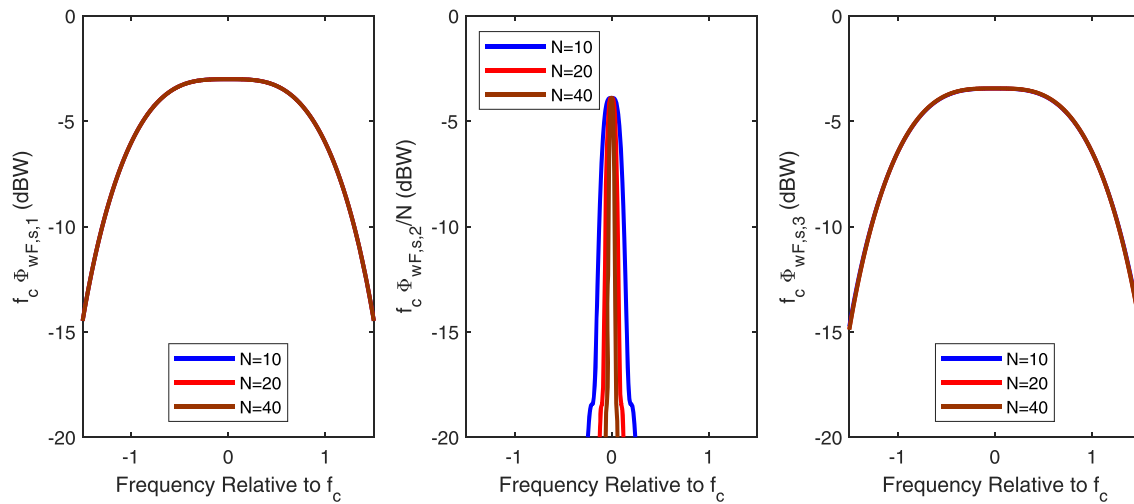


FIGURE 5 Unit-power PSDs for noise terms in dual-channel semicodeless processing after signal wipeoff in signal tracking; observe the different normalization in the center graphic [Color figure can be viewed at wileyonlinelibrary.com and www.ion.org]

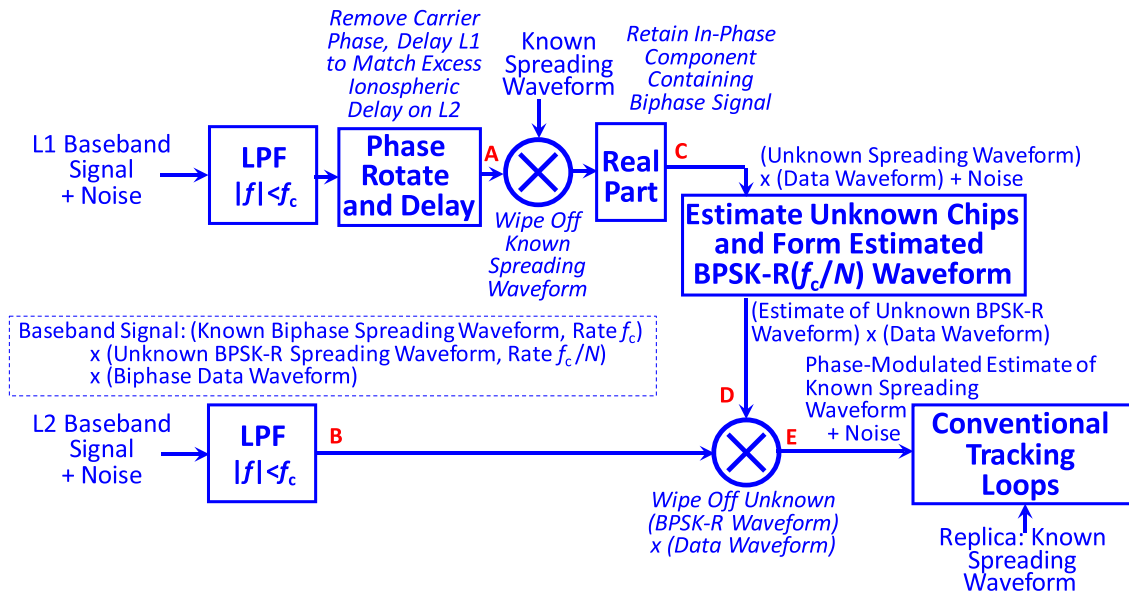


FIGURE 6 Model of dual-channel soft-decision semicodeless processing [Color figure can be viewed at wileyonlinelibrary.com and www.ion.org]

estimates the unknown spreading symbols. The signal enhancement processing in Figure 6 is similar to that for semicodeless processing: wiping off the higher rate known spreading waveform to reduce the signal bandwidth to that of the lower rate spreading waveform, then taking the real part to eliminate noise in phase quadrature to the signal. However, instead of lowpass filtering to remove noise outside the reduced signal bandwidth, this enhancement processing estimates the unknown BPSK-R spreading waveform having chip rate f_c/N^4 , using synchronous integrate-and-dump operations to

form a soft-decision estimate of each chip value. This architecture appears to be similar to what is called “Soft-Decision Z-Tracking” in Woo.⁴

The waveform at Point C is the same as in semicodeless processing and is thus described by Equations (24) and (25). Estimation of unknown chip values using the waveform at Point C is assumed synchronized to the spreading symbols. Without loss of generality, define the time origin to span a specific spreading symbol $-NT_c/2 < t \leq NT_c/2$ where $T_c = 1/f_c$. The input waveform during that time is $a_0 d_0 + w_c(t)$, $-NT_c$

$/2 < t \leq NT_c/2$ where a_0 is the unknown chip value, d_0 is the unknown data bit value, and $w_C(t)$ is defined in the previous section.

As indicated above, what is being estimated is the product of the unknown chip value and the unknown data bit value. This estimate $\widehat{a_0 d_0}$ is formed by

$$\widehat{a_0 d_0} = \frac{1}{NT_c} \int_{-NT_c/2}^{NT_c/2} [a_0 d_0 + w_C(t)] dt. \quad (34)$$

Its mean is

$$E\{\widehat{a_0 d_0}\} = a_0 d_0 \quad (35)$$

so the estimate is unbiased. The error, or the output noise, associated with the estimate is

$$\frac{1}{NT_c} \int_{-NT_c/2}^{NT_c/2} w_C(t) dt. \quad (36)$$

Its variance is given by

$$\begin{aligned} \text{Var}\{\widehat{a_0 d_0}\} &= E\left\{\left(\frac{1}{NT_c}\right)^2 \int_{-NT_c/2}^{NT_c/2} \int_{-NT_c/2}^{NT_c/2} w_C(t_1) w_C(t_2) dt_1 dt_2\right\} \\ &= \left(\frac{1}{NT_c}\right)^2 \int_{-NT_c/2}^{NT_c/2} \int_{-NT_c/2}^{NT_c/2} R_{w_C}(t_2 - t_1) dt_1 dt_2 \end{aligned} \quad (37)$$

where $R_{w_C}(\tau)$ is the ACF of $w_C(t)$, given in Equation (25).

Using results from page 324 of Papoulis⁵ and Equation (25), Equation (37) simplifies to

$$\text{Var}\{\widehat{a_0 d_0}\} = \frac{f_c N_0}{NT_c} \int_{-NT_c}^{NT_c} \left[1 - \frac{|\tau|}{NT_c}\right] \text{sinc}(2\pi f_c \tau) \overline{R}_y(\tau) d\tau. \quad (38)$$

Substituting Equation (5) and using $T_c = 1/f_c$ yields

$$\begin{aligned} \text{Var}\{\widehat{a_0 d_0}\} &= \frac{N_0 (f_c)^2}{N} \int_{-T_c}^{T_c} \left[1 - \frac{|\tau| f_c}{N}\right] \\ &\quad \text{sinc}(2\pi f_c \tau) [1 - |\tau| f_c] d\tau = N_0 \frac{f_c}{N \Omega(N)} \end{aligned} \quad (39)$$

where

$$\Omega(N) = \left[\int_{-1}^1 \left[1 - \frac{|u|}{N}\right] \text{sinc}(2\pi u) [1 - |u|] du \right]^{-1} \quad (40)$$

is the soft-decision gain, relative to semicodeless processing analyzed in the previous subsection.

Table 1 provides numerical values for $\Omega(N)$. For large values of N , $\Omega(N) \cong \left[\int_{-1}^1 \text{sinc}(2\pi u) [1 - |u|] du \right]^{-1} = 2.2148$.

For large N , the errors associated with estimates of sequential chip values are approximately uncorrelated, so the soft decision estimate is modeled as the true BPSK-R waveform with chip rate f_c/N plus a BPSK-R noise waveform with chip rate f_c/N , having zero mean and average power given by Equation (39).

The waveform after signal enhancement for soft-decision semicodeless processing (indicated by the “d” in the subscript) is

$$\begin{aligned} r_{D,d}(t) &\cong \phi \alpha_1 \sum_{k=-\infty}^{\infty} a_k g_{NT_c}(t - kNT_c) \\ &\quad \sum_{j=-\infty}^{\infty} d_j g_{DT_c}(t - jDT_c) + w_{D,d}(t) \end{aligned} \quad (41)$$

where

$$w_{D,d}(t) = \sum_{k=-\infty}^{\infty} \nu_k g_{NT_c}(t - kNT_c) \quad (42)$$

with $E\{\nu_k\} = 0$, $\text{Var}\{\nu_k\} = N_0 \frac{f_c}{NT(N)}$, and the ν_k mutually orthogonal. The first term in Equation (41) is the signal term, with ACF

$$\phi^2 \alpha_1^2 \text{tri}_{N/f_c}(\tau). \quad (43)$$

The ACF of the noise term, $w_{D,d}(t)$, is

TABLE 1 Numerical values of Equation (40)

N	$\Omega(N)$
10	2.2399
20	2.2273
30	2.2231
40	2.2210
50	2.2198
1000	2.2150
10^6	2.2148

$$R_{w_{D,d}}(\tau) = N_0 \frac{f_c}{N\Omega(N)} \text{tri}_{N/f_c}(\tau). \quad (44)$$

Its noise power is $N_0 \frac{f_c}{N\Omega(N)}$. Compared with the result for semicodeless processing, where $w_{D,s}(t)$ has power $f_c N_0 / N$, the power of $w_{D,d}(t)$ in soft-decision semicodeless processing is reduced by $\Omega(N)$, a reduction of approximately 3.5 dB based on the numerical results in Table 1. Thus, soft-decision semicodeless processing provides a performance enhancement on the order of 3.5 dB greater than semicodeless processing.

The final multiplication in Figure 6 then wipes off the estimated unknown spreading waveform and the data modulation, leaving the waveform at Point E

$$w_{F,d,2}(t) \cong \left[\phi \alpha_2 \sum_{k=-\infty}^{\infty} a_k g_{NT_c}(t - kNT_c) \sum_{j=-\infty}^{\infty} d_j g_{DT_c}(t - jDT_c) e^{i\theta_2(t)} \right] w_{D,d}(t)$$

$$w_{F,d,3}(t) \cong w_B(t) w_{D,d}(t) \sum_{m=-\infty}^{\infty} b_m g_{T_c}(t - mT_c).$$

The first term in Equation (46) is a slowly varying complex sinusoid having power

$$(\phi^2 \alpha_1 \alpha_2)^2 = (N_0)^2 \phi^4 (C/N_0)_1 (C/N_0)_2 \quad (47)$$

$$r_{E,d}(t) = r_B(t) r_{D,d}(t) \cong \left[\phi \alpha_1 \sum_{k=-\infty}^{\infty} a_k g_{NT_c}(t - kNT_c) \sum_{j=-\infty}^{\infty} d_j g_{DT_c}(t - jDT_c) + w_{D,d}(t) \right]$$

$$\times \left[\phi \alpha_2 \sum_{k=-\infty}^{\infty} a_k g_{NT_c}(t - kNT_c) \sum_{m=-\infty}^{\infty} b_m g_{T_c}(t - mT_c) \sum_{j=-\infty}^{\infty} d_j g_{DT_c}(t - jDT_c) e^{i\theta_2(t)} + w_B(t) \right] \quad (45)$$

$$= \phi^2 \alpha_1 \alpha_2 \sum_{m=-\infty}^{\infty} b_m g_{T_c}(t - mT_c) e^{i\theta_2(t)} + w_B(t) \left[\phi \alpha_1 \sum_{k=-\infty}^{\infty} a_k g_{NT_c}(t - kNT_c) \sum_{j=-\infty}^{\infty} d_j g_{DT_c}(t - jDT_c) \right]$$

$$+ \left[\phi \alpha_2 \sum_{k=-\infty}^{\infty} a_k g_{NT_c}(t - kNT_c) \sum_{m=-\infty}^{\infty} b_m g_{T_c}(t - mT_c) \sum_{j=-\infty}^{\infty} d_j g_{DT_c}(t - jDT_c) e^{i\theta_2(t)} \right] w_{D,d}(t) + w_B(t) w_{D,d}(t).$$

This result leads to the conventional process of tracking the carrier phase of a known BPSK-R signal in additive noise.

The conventional tracking loops after Point E wipe off $\sum_{m=-\infty}^{\infty} b_m g_{T_c}(t - mT_c)$ from $r_{E,d}(t)$. The waveform at this Point F is

$$r_{F,d}(t) = r_{E,d}(t) \sum_{m=-\infty}^{\infty} b_m g_{T_c}(t - mT_c) \cong \phi^2 \alpha_1 \alpha_2 e^{i\theta_2(t)} \quad (46)$$

$$+ w_{F,d,1}(t) + w_{F,d,2}(t) + w_{F,d,3}(t)$$

where

$$w_{F,d,1}(t) \cong w_B(t) \left[\phi \alpha_1 \sum_{k=-\infty}^{\infty} a_k g_{NT_c}(t - kNT_c) \sum_{j=-\infty}^{\infty} d_j g_{DT_c}(t - jDT_c) \right]$$

summed with three mutually uncorrelated zero-mean noise terms having respective approximate ACFs

$$R_{w_{F,d,1}}(\tau) \cong \phi^2 \alpha_1^2 \text{tri}_{1/f_c}(\tau) R_{w_B}(\tau) \quad (48)$$

$$= 2 \phi^2 (C/N_0)_1 f_c (N_0)^2 \text{tri}_{1/f_c}(\tau) \text{sinc}(2\pi f_c \tau)$$

$$R_{w_{F,d,2}}(\tau) \cong \phi^2 \alpha_2^2 \text{tri}_{N/f_c}(\tau) R_{w_{D,d}}(\tau) \quad (49)$$

$$= \phi^2 (C/N_0)_2 (N_0)^2 \frac{f_c}{N\Omega(N)} [\text{tri}_{N/f_c}(\tau)]^2$$

$$R_{w_{F,d,3}}(\tau) = R_{w_B}(\tau) R_{w_{D,d}}(\tau) \bar{R}_y(\tau) = \frac{2(f_c N_0)^2}{N\Omega(N)} \text{sinc}(2\pi f_c \tau) \text{tri}_{N/f_c}(\tau) \text{tri}_{1/f_c}(\tau) \cong (f_c N_0)^2 (2/N) \text{sinc}(2\pi f_c \tau) \text{sinc}(2\pi f_c \tau / N) \text{tri}_{1/f_c}(\tau). \quad (50)$$

These ACFs and the corresponding PSDs can be computed numerically: $\Phi_{w_{F,d,1}}(f) = F\{R_{w_{F,d,1}}(\tau)\}$, $\Phi_{w_{F,d,2}}(f) = F\{R_{w_{F,d,2}}(\tau)\}$, and $\Phi_{w_{F,d,3}}(f) = F\{R_{w_{F,d,3}}(\tau)\}$. Figure 7 compares the shapes of the PSDs numerically computed from Fourier transforms of Equations (48), (49), and (50). Clearly, $w_{F,d,2}(t)$ has much narrower bandwidth than the other noise terms, concentrating its power in band center.

4 | PERFORMANCE ANALYSIS

Dual-channel codeless and semicodeless processing are employed primarily to allow tracking of the L2 carrier. As shown in Betz,⁶ the effective C/N_0 at the input to the tracking loop(s) is a suitable performance metric for carrier tracking and is thus assessed at Point E in Figures 2, 4, and 6. This section assembles expressions for effective C/N_0 based on results in the previous section.

4.1 | Performance of dual-channel codeless processing

Referring to Figure 2, the effective C/N_0 for a phase-locked loop tracking the signal in $r_{E,c}(t)$ is determined by the ratio of the power in the slowly varying sinusoid, given by Equation (19), divided by the total noise PSD at Point E, (23), evaluated at $f = 0$. (Observe from Figure 3 that the noise PSD terms are relatively flat over the tens of hertz used to track the sinusoid, so the noise PSD at this point is approximated as white, and its peak value at $f = 0$ is used.) Since $\Phi_{w_{E,c}}(0) = \int R_{w_{E,c}}(\tau) d\tau$, the effective C/N_0 at Point E for dual-channel codeless processing is

$$(C/N_0)_c \cong (N_0)^2 \phi^4 (C/N_0)_1 (C/N_0)_2 \times \left[(N_0)^2 [2(C/N_0)_1 + (C/N_0)_2] (f_c \phi^2) \int_{-\infty}^{\infty} \text{tri}_{1/f_c}(\tau) \text{sinc}(2\pi f_c \tau) d\tau + (N_0)^2 f_c^2 \int_{-\infty}^{\infty} \text{sinc}^2(2\pi f_c \tau) d\tau \right]^{-1} \quad (51)$$

Using $\int_{-\infty}^{\infty} \text{sinc}^2(2\pi f_c \tau) d\tau = 1/(2f_c)$ and

$$\begin{aligned} \int_{-\infty}^{\infty} \text{tri}_{1/f_c}(\tau) \text{sinc}(2\pi f_c \tau) d\tau &= (2/f_c) \int_0^1 [1-u] \text{sinc}(2\pi u) du \\ &= (2/f_c) \int_0^1 \text{sinc}(2\pi u) du \cong 0.4515/f_c \end{aligned}$$

in Equation (51) yields

$$\begin{aligned} (C/N_0)_c &\cong \frac{\phi^4 (C/N_0)_1 (C/N_0)_2}{[2(C/N_0)_1 + (C/N_0)_2] (f_c \phi^2) (0.4514/f_c) + 0.4916 f_c} \\ &= \frac{2.0342 \phi^4 (C/N_0)_1 (C/N_0)_2 / f_c}{1.8365 \phi^2 (C/N_0)_1 / f_c + 0.9182 \phi^2 (C/N_0)_2 / f_c + 1} \quad (52) \end{aligned}$$

4.2 | Performance of dual-channel semicodeless processing

Referring to Figure 4, the effective C/N_0 for tracking of the signal in $r_{E,s}(t)$ is determined by the ratio of the power in the slowly varying sinusoid, given by Equation (47), divided by the sum of the areas under the correlation functions (31), (32), and (33) as in Equation (51), yielding

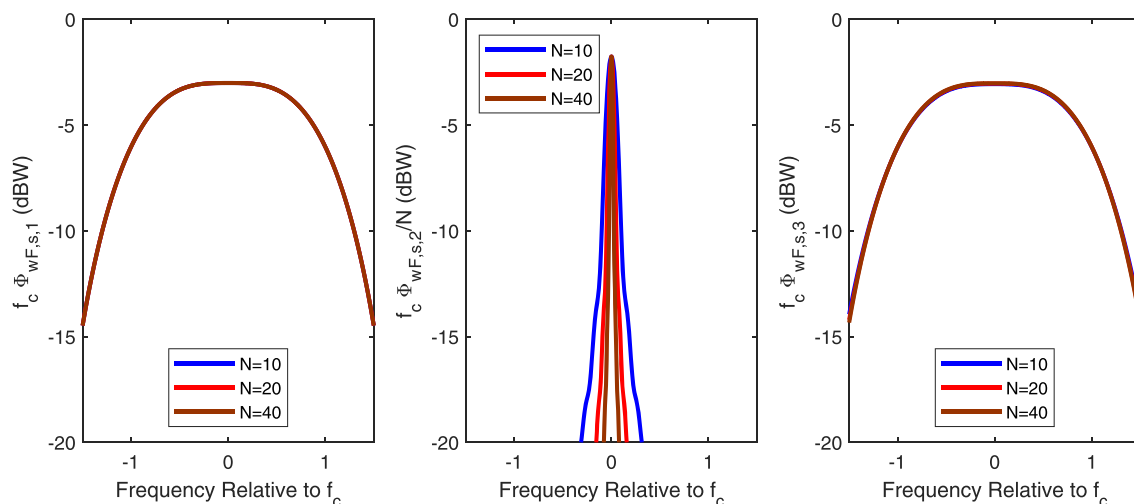


FIGURE 7 PSDs for noise terms in dual-channel soft-decision semicodeless processing after signal wipeoff in signal tracking; first and third are unit-power while the center has power $1/N$ [Color figure can be viewed at wileyonlinelibrary.com and www.ion.org]

$$\begin{aligned}
(C/N_0)_s \cong & 0.9028\phi^4 (C/N_0)_1 (C/N_0)_2 \\
& \left[1.8056 \phi^2 (C/N_0)_1 \int_{-\infty}^{\infty} f_c \text{tri}_{1/f_c}(\tau) \text{sinc}(2\pi f_c \tau) d\tau \right. \\
& + \phi^2 (C/N_0)_2 \int_{-\infty}^{\infty} (f_c/N) \text{tri}_{N/f_c}(\tau) \text{sinc}(2\pi f_c \tau/N) d\tau \\
& \left. + (2f_c/N) \int_{-\infty}^{\infty} f_c \text{sinc}(2\pi f_c \tau) \text{sinc}(2\pi f_c \tau/N) \text{tri}_{1/f_c}(\tau) d\tau \right]^{-1}.
\end{aligned} \quad (53)$$

(Observe from Figure 5 that the noise PSD terms are relatively flat over the tens of hertz used to track the sinusoid, so the noise PSD at this point is approximated as white, and its peak value at $f=0$ is used. The PSD at $f=0$ is equal to the area under the correlation function.)

Numerical evaluation shows that the integrals in Equation (53) are virtually invariant over the values of N being considered, yielding the approximation

$$\begin{aligned}
(C/N_0)_s \cong & \frac{0.9028 \phi^4 (C/N_0)_1 (C/N_0)_2}{1.8056 \phi^2 (C/N_0)_1 0.50 + \phi^2 (C/N_0)_2 0.45 + (2f_c/N) 0.50} \\
\cong & \frac{0.9028 N \phi^4 (C/N_0)_1 (C/N_0)_2 / f_c}{0.9028 N \phi^2 (C/N_0)_1 / f_c + 0.4500 N \phi^2 (C/N_0)_2 / f_c + 1}.
\end{aligned} \quad (54)$$

4.3 | Performance of dual-channel soft-decision semicodeless processing

Referring to Figure 6, the effective C/N_0 for tracking of the signal in $r_{E,d}(t)$ is determined by the ratio of the power in the slowly varying sinusoid, given by Equation (47), divided by the sum of the areas under the correlation functions (48), (49), (50), as in Equations (51) and (53), yielding

$$\begin{aligned}
(C/N_0)_s \cong & \phi^4 (C/N_0)_1 (C/N_0)_2 \left[2 \phi^2 (C/N_0)_1 \int_{-\infty}^{\infty} f_c \text{tri}_{1/f_c}(\tau) \text{sinc}(2\pi f_c \tau) d\tau + \phi^2 (C/N_0)_2 \frac{1}{\Omega(N)} \right. \\
& \left. \int_{-\infty}^{\infty} (f_c/N) [\text{tri}_{N/f_c}(\tau)]^2 d\tau + \frac{2f_c}{N\Gamma(N)} \int_{-\infty}^{\infty} f_c \text{sinc}(2\pi f_c \tau) \text{tri}_{N/f_c}(\tau) \text{tri}_{1/f_c}(\tau) d\tau \right]^{-1}
\end{aligned} \quad (55)$$

(Observe from Figure 7 that the noise PSD terms are relatively flat over the tens of hertz used to track the sinusoid, so the noise PSD at this point is approximated as white, and its peak value at $f=0$ is used. The PSD at $f=0$ is equal to the area under the correlation function.)

Numerical evaluation shows that the integrals in Equation (55) are virtually invariant over the values of N being considered, yielding the approximation

$$\begin{aligned}
(C/N_0)_s \cong & \frac{\phi^4 (C/N_0)_1 (C/N_0)_2}{2 \phi^2 (C/N_0)_1 0.45 + \phi^2 (C/N_0)_2 0.73/\Omega(N) + \frac{2f_c}{N\Omega(N)} 0.45} \\
\cong & \frac{1.1111 N \Gamma(N) \phi^4 (C/N_0)_1 (C/N_0)_2 / f_c}{N \Gamma(N) \phi^2 (C/N_0)_1 / f_c + 0.8111 N \phi^2 (C/N_0)_2 / f_c + 1}.
\end{aligned} \quad (56)$$

4.4 | Summary of performance results

The results in this section show that the performance of all three types of codeless and semicodeless processing considered in this paper is expressed using the same parametric form,

$$(C/N_0)_{c,s,d} = \frac{\gamma (C/N_0)_1 (C/N_0)_2}{\eta (C/N_0)_1 + \lambda (C/N_0)_2 + 1} \quad (57)$$

having bilinear upper bound

$$(C/N_0)_{c,s,d} < \gamma (C/N_0)_1 (C/N_0)_2 \quad (58)$$

with approximate coefficients, all positive, listed in Table 2.

Squaring loss, defined in Woo,⁴ is

$$\frac{(C/N_0)_2}{(C/N_0)_{c,s,d}} = \frac{\eta (C/N_0)_1 + \lambda (C/N_0)_2 + 1}{\gamma (C/N_0)_1}. \quad (59)$$

TABLE 2 Approximate coefficients for performance of dual-channel codeless and semicodeless processing

Dual-Channel Processing Type	γ	η	λ
Codeless	$2.0342 \phi^4 / f_c$	$1.8365 \phi^2 / f_c$	$0.9182 \phi^2 / f_c$
Semicodeless	$0.9028 N \phi^4 / f_c$	$0.9028 N \phi^2 / f_c$	$0.4500 N \phi^2 / f_c$
Soft-decision semicodeless	$1.1111 N \Gamma(N) \phi^4 / f_c$	$N \Omega(N) \phi^2 / f_c$	$0.8111 N \phi^2 / f_c$

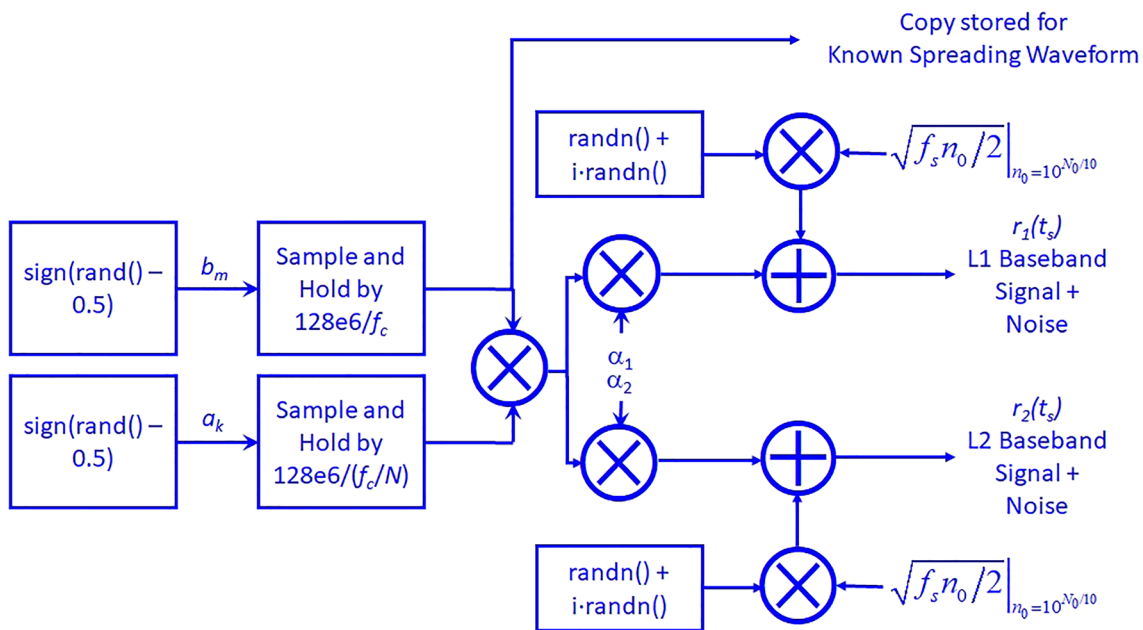
The effective C/N_0 decreases with higher chip rates. Codeless performance is insensitive to N , since this processing does not exploit signal structure other than the fact that the signal is biphasic. However, the effective C/N_0 from both types of semicodeless processing increases with N , when the unknown spreading waveform has lower chip rate. Soft-decision semicodeless outperforms semicodeless by as much as $\Omega(N)$, approaching 4 dB.

5 | COMPUTER SIMULATION

The MATLAB simulation developed to crosscheck the analytical results consists of a signal generator followed by the receiver processing. The signal generator is shown in Figure 8. First, a baseband DSSS signal is generated corresponding to Equation (1). The chip values a_k and b_m are produced using a random number generator, yielding uncorrelated and identically distributed values of ± 1 . The chip rate of b_m is $f_c = 10.23$ MHz, while the chip rate of a_k is f_c/N . The chip sequences are upsampled with sample and hold to a sampling rate of $f_s = 128$ megasamples

per second (Ms/s), selected to avoid commensurate sampling, forming BPSK-R spreading modulations. Without loss of generality, the data message bits d_j are set to unity.

A copy of the upsampled signal $\sum_{m=-\infty}^{\infty} b_m \text{rect}_{T_c}(t - mT_c)$ is stored for later use in the processing. The upsampled signals $\sum_{k=-\infty}^{\infty} a_k \text{rect}_{NT_c}(t - mNT_c)$ and $\sum_{m=-\infty}^{\infty} b_m \text{rect}_{T_c}(t - mT_c)$ are then multiplied together sample-by-sample to complete formation of the sampled representation of the baseband signal (1), with discrete sample times t_s spaced by $1/f_s$. Two copies of the sampled signal, one for L1 and the other for L2, are created, each scaled by applying the appropriate amplitude over the precorrelation bandwidth of ± 15.345 MHz. Without loss of generality, a carrier phase is pseudorandomly applied only to the L2 signal. No transmit filter is applied to the signals since the precorrelation filter bandlimits the signals. Samples of mutually uncorrelated complex Gaussian white noise for the L1 and L2 waveforms are generated using the MATLAB function `randn()` at the sampling rate f_s and scaled to generate noise at the appropriate PSD N_0 . The complex noise time series are added to the L1 and L2

**FIGURE 8** Signal generation for computer simulation [Color figure can be viewed at wileyonlinelibrary.com and www.ion.org]

signals to form sampled versions of Equation (3). The resulting L1 and L2 baseband waveforms are sampled versions of the inputs on the left-hand side of Figures 1 through 4.

The receiver processing follows the models illustrated in Figures 1 through 4. Lowpass filter coefficients are generated for a 2048-tap finite impulse response (FIR) filter with a stop frequency of f_c using the MATLAB `fir1()` function, ensuring linear phase. These filter coefficients are used by the MATLAB function `filter()` to lowpass filter the input L1 and L2 baseband signals and noise. The initial 1024 samples output from the `filter()` function are truncated to maintain synchronization of all signals.

Continuing along the L1 path, since the L1 baseband signal was synthesized without delay or phase rotation, these parameters do not need to be removed in the simulation. The result is the waveforms at Point A and Point B in all the processing approaches. Beyond this point, the processing approaches differ, and different simulations are then performed as described below.

To implement the codeless processing in Figure 2, the real portion of the waveform at Point A is taken, creating the waveform at D, which is then multiplied sample-by-sample with the waveform at Point B to create the waveform at Point E.

For the semicodeless processing in Figure 4, the waveform at Point A is multiplied sample-by-sample with the copy of the known spreading waveform created during signal generation, and the real part of the resulting waveform is retained, creating the waveform at Point C. The

waveform at Point C is lowpass filtered, as shown in Figure 9, once again using the MATLAB `filter()` function with low pass filter coefficients generated for a FIR filter, with a stop frequency of f_c/N using the MATLAB `fir1()` function. A 2048-tap filter is used, and the initial 1024 output samples are truncated to produce the sampled signal at Point D. The truncation removes the constant FIR filter delay and retains synchronization with the L2 signal path. The waveform at Point D is then sample-by-sample multiplied with the signal from Point B to arrive at the signal at Point E.

For the soft-decision semicodeless processing shown in Figure 6, the waveform up to Point D is the same as in the semicodeless processing. Then, a soft decision estimate of the unknown spreading waveform is formed using the processing shown in Figure 10, yielding the waveform at Point D in Figure 6. This waveform is then sample-by-sample multiplied with the waveform from Point B to produce the waveform at Point E.

The simulation then estimates the effective C/N_0 in the waveforms at Point E. For codeless processing, the C/N_0 of the resulting constant (since perfect frequency alignment is used in the simulation) in noise is then estimated directly. For semicodeless processing without and with soft decisions, the waveform at Point E is a DSSS signal in noise. Effective C/N_0 for this waveform is estimated from the dot product of a replica of the DSSS signal and the corresponding waveform at Point E, using sequential dot products each computed over 1-ms intervals. The effective C/N_0 estimate is

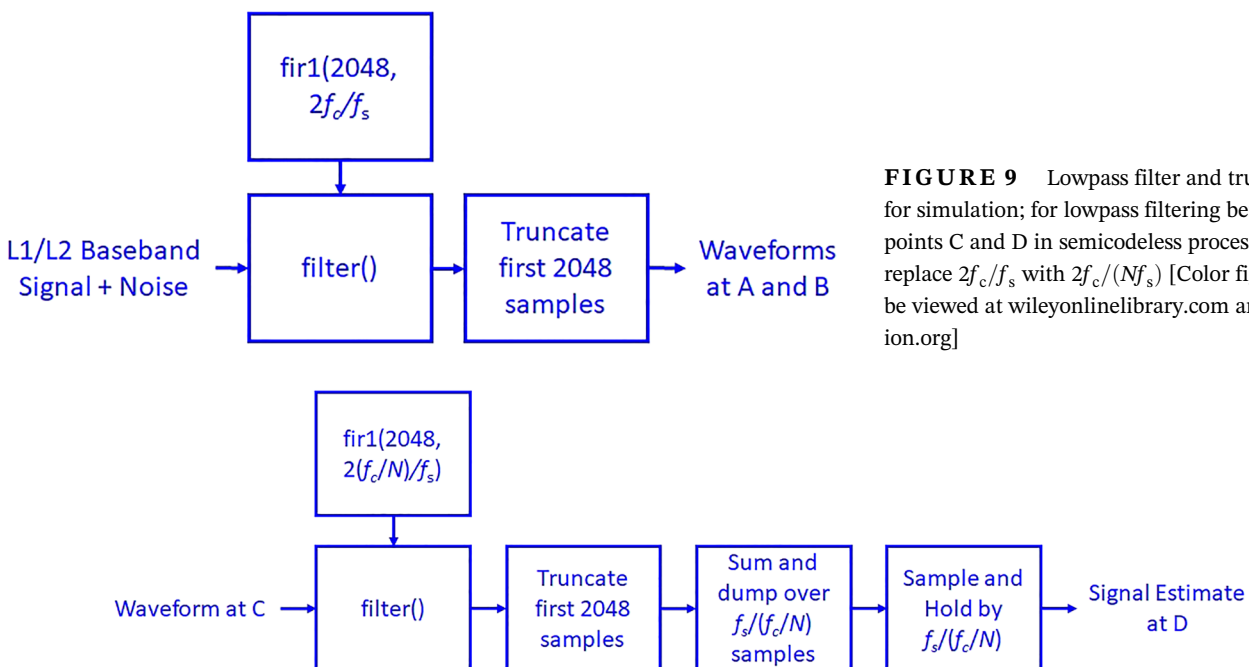


FIGURE 9 Lowpass filter and truncation for simulation; for lowpass filtering between points C and D in semicodeless processing, replace $2f_c/f_s$ with $2f_c/(Nf_s)$ [Color figure can be viewed at wileyonlinelibrary.com and www.ion.org]

FIGURE 10 Soft-decision estimation of the unknown signal component [Color figure can be viewed at wileyonlinelibrary.com and www.ion.org]

$$(\widehat{C/N_0})_{\text{eff}} = \hat{\mu}^2 \hat{\sigma}^2 \quad (60)$$

where $\hat{\mu}$ and $\hat{\sigma}^2$ are, respectively, the sample mean and sample variance of the real parts of the dot products, each computed over 30,000 sequential 1-ms intervals using the MATLAB functions `mean()` and `var()`.

6 | NUMERICAL RESULTS

Numerical results from the analytical model and simulation are provided in this section for a known signal component chip rate of 10.23 MHz, with signal powers defined over ± 15.345 MHz. Figure 11 shows results for codeless processing. The dashed line is the bilinear upper bound, while there are three almost indistinguishable solid lines: the upper one for $(C/N_0)_2 = 2 \times (C/N_0)_1$, the center one for $(C/N_0)_2 = (C/N_0)_1$, and the lower one for $(C/N_0)_2 = (C/N_0)_1/2$.

Corresponding simulation results are plotted at discrete points, with excellent correspondence between analytical and simulation results. Clearly, for these numerical values, the bilinear upper bound is very tight, and the performance depends almost entirely on the product of the input C/N_0 values, with little difference if one is slightly larger or smaller than the other. Input C/N_0 values must approach 55 dB-Hz in each channel in order to obtain the desirable situation of codeless C/N_0 greater than 40 dB-Hz—desirable since this C/N_0 is large enough for ambiguity resolution and for reliable tracking loop lock.

Results for semicodeless processing are portrayed in Figure 12. The dashed lines are bilinear upper bounds,

while there are groups of three almost indistinguishable solid lines: the upper one for $(C/N_0)_2 = 2 \times (C/N_0)_1$, the center one for $(C/N_0)_2 = (C/N_0)_1$, and the lower one for $(C/N_0)_2 = (C/N_0)_1/2$. Simulation results are provided at discrete points, with excellent correspondence between analytical and simulation results. The semicodeless numerical results are distinctly different for different values of N , the ratio between the chip rate of the known signal component and the chip rate of the unknown signal component. All the effective C/N_0 values shown are significantly larger than corresponding values from codeless processing, showing the benefit of semicodeless processing when N is large. Even for a signal design with $N = 10$, input C/N_0 values slightly greater than 50 dB-Hz at each input yield the desirable situation of codeless C/N_0 greater than 40 dB-Hz. The semicodeless C/N_0 increases with larger values of N , showing the advantage of a slower chip rate for the unknown signal component. While the semicodeless C/N_0 tracks the bilinear upper bound closely for small and moderate input C/N_0 values, at larger input C/N_0 values the semicodeless C/N_0 falls below the bilinear upper bound. The departure from the bilinear upper bound is more pronounced for larger values of N . Other results, not shown here, indicate divergence between curves for the same value of N and the same product of $(C/N_0)_1(C/N_0)_2$, but different ratios between $(C/N_0)_1$ and $(C/N_0)_2$ as the input C/N_0 values increase beyond those plotted here.

Figure 13 shows results for soft decision semicodeless processing, with the dashed lines and the triplets of solid lines having the same meaning as in the other figures. Simulation results are provided at discrete points, with about 1 dB offset between analytical and simulation

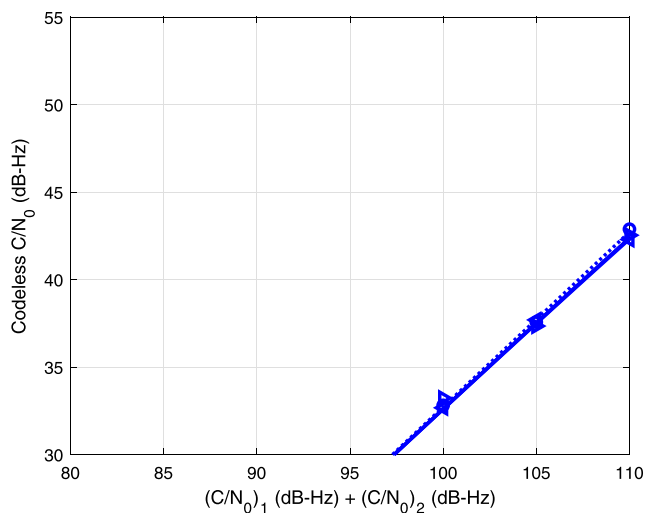


FIGURE 11 Dual-channel codeless C/N_0 numerical (lines) and simulation (symbols) results [Color figure can be viewed at wileyonlinelibrary.com and www.ion.org]

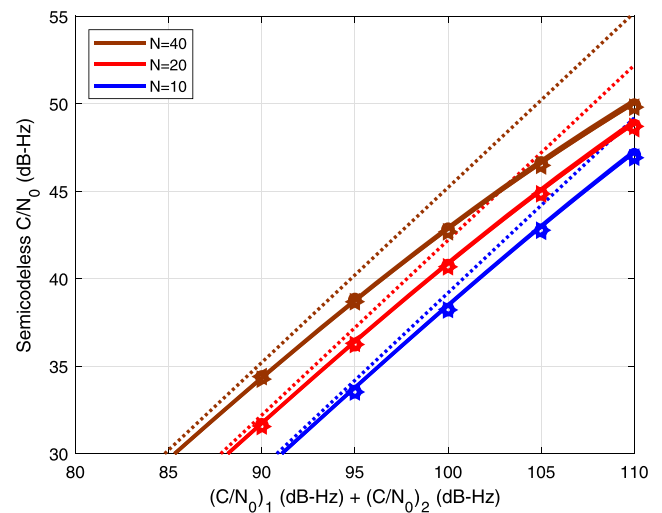


FIGURE 12 Dual-channel semicodeless C/N_0 numerical (lines) and simulation (symbols) results [Color figure can be viewed at wileyonlinelibrary.com and www.ion.org]

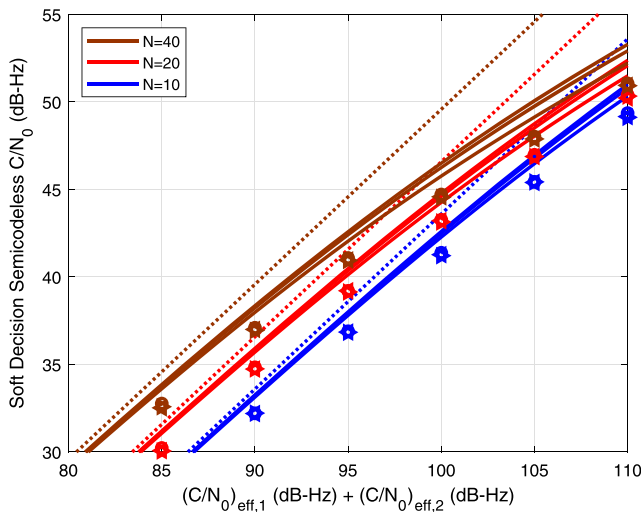


FIGURE 13 Dual-channel soft-decision semicodeless C/N_0 numerical (lines) and simulation (symbols) results [Color figure can be viewed at wileyonlinelibrary.com and www.ion.org]

results, possibly reflecting unmodeled losses in the simulation of soft decision processing. These results are qualitatively similar to those for semicodeless, except the C/N_0 is several dB larger for small and moderate input C/N_0 values, showing the performance advantage of the soft decision processing. With larger input C/N_0 values, the performance benefits of the soft decision processing diminish relative to standard semicodeless processing.

TABLE 3 Comparison of analytical results in this paper with corresponding results in Woo⁴ for $N = 20$ and $(C/N_0)_2 = 0.5 \times (C/N_0)_1$

L2 C/N_0 (dB-Hz)	Architecture	Squaring Loss (dB)
39	Dual-channel codeless	25.3
	L1 \times L2 cross-correlation ⁴	28
	Dual-channel semicodeless	15.8
	P-code aided cross-correlation ⁴	15
	Dual-channel soft-decision semicodeless	11.4
	Soft-decision Z-tracking ⁴	12
	Maximum <i>a posteriori</i> ⁴	11
42	Dual-channel codeless	22.3
	L1 \times L2 cross-correlation ⁴	25
	Dual-channel semicodeless	12.8
	P-code aided cross-correlation ⁴	12
	Dual-channel soft-decision semicodeless	9.0
	Soft-decision Z-tracking ⁴	9.5
	Maximum <i>a posteriori</i> ⁴	8

Analytical results in this paper can be compared with corresponding results in Woo,⁴ for the specific situation addressed in Woo⁴: $N = 20$ and $(C/N_0)_2 = 0.5 \times (C/N_0)_1$. Table 3 shows the comparison, using squaring loss as defined in Equation (59): the difference (in dB) between the L2 C/N_0 and the output C/N_0 . Dual-channel codeless processing has approximately 3 dB less squaring loss than L1 \times L2 cross-correlation in Woo,⁴ presumably since dual-channel cross-correlation processing discards half the noise in the L1 channel by taking the real part. Squaring losses from dual-channel semicodeless processing are only 0.8 dB different from those reported for P-code aided cross-correlation.⁴ Squaring losses for dual-channel soft-decision semicodeless are within 1 dB of those reported for both soft-decision Z-tracking and maximum *a posteriori* in Woo.⁴ Moreover, the changes in squaring loss with changes in L2 C/N_0 are very similar for the architectures explored in this paper and corresponding architectures in Woo.⁴

7 | SUMMARY



The performance of three different processing techniques has been quantified for receiving a common signal on two carrier frequencies that has an unknown spreading waveform. It is assumed that the signal on one carrier frequency can be tracked perfectly, through tracking of a second known signal on the same carrier. The processing tracks the carrier phase of the signal on the second carrier frequency. Dual-channel codeless processing only exploits the biphasic nature of the signal, while dual-channel semicodeless processing also exploits the hypothesis that the signal is the product of a known spreading waveform and an unknown spreading waveform at a known lower chip rate. Dual-channel soft-decision semicodeless processing also exploits the hypothesized spreading modulation of the unknown spreading waveform. Performance of all three processing techniques is described by a common parametric form, although the parameter values differ for the different processing techniques. In all cases, the performance is better when the chip rate of the known spreading waveform is smaller, and the performance of dual-channel semicodeless techniques is also better when the chip rate of the unknown spreading waveform is smaller. Close correspondence between analytical and simulation results provides great confidence in the analytical results.

ACKNOWLEDGMENTS

Thanks to Dr. Sharon Marroquin and Ryan Cassel for their helpful reviews of this paper. The work was supported by the U.S. Air Force under contract

no. FA8702-19-C-0001. The authors also thank the reviewers for perceptive and helpful suggestions.

ORCID

John W. Betz  <https://orcid.org/0000-0002-3594-594X>
Alessandro P. Cerruti  <https://orcid.org/0000-0002-2989-9967>

REFERENCES

1. Lorenz R, Gourevitch S. The Z-12 Performance advantage. *Proceedings of the 1995 National Technical Meeting of The Institute of Navigation*. Anaheim, California; January 1995:439-444.
2. Ripley M, Cooper I, Daly P, Silvestrin P. Development of a dual-frequency GNSS receiver for scientific applications. *Proceedings of the 11th International Technical Meeting of the Satellite Division of The Institute of Navigation (ION GPS 1998)*. Nashville, TN; September 1998:1645-1654.
3. Jung H, Psiaki ML, Powell SP. Kalman-filter-based semi-codeless tracking of weak dual-frequency GPS signals. *Proceedings of the 16th International Technical Meeting of the Satellite Division of The Institute of Navigation (ION GPS/GNSS 2003)*. Portland, OR; September 2003:2515-2523.
4. Woo KT. Optimum semicodeless carrier-phase tracking of L2. *Navigation*. 2000;47:82-99.
5. Papoulis A. *Probability, Random Variables, and Stochastic Processes*. New York: McGraw-Hill; 1965.
6. Betz JW. *Engineering Satellite-Based Navigation and Timing: Global Navigation Satellite Systems, Signals, and Receivers*. Piscataway, NJ: Wiley-IEEE Press; 2015.

How to cite this article: Betz JW, Cerruti AP. Performance of dual-channel codeless and semicodeless processing. *NAVIGATION*. 2020;67: 109–128. <https://doi.org/10.1002/navi.347>

APPENDIX A

EXAMPLE DERIVATION

This paper contains derivations of many correlation functions; an example derivation of Equation (20) is provided here for the correlation function of $w_{E,c,1}(t) = \phi \alpha_1 y(t) w_B(t)$.

$$\begin{aligned} R_{E,c,1}(\tau) &= E\{w_{E,c,1}(t)w_{E,c,1}(t-\tau)\} \\ &= E\{\phi \alpha_1 y(t)w_B(t)\phi \alpha_1 y(t-\tau)w_B(t-\tau)\} \\ &= \phi^2 \alpha_1^2 E\{y(t)w_B(t)y(t-\tau)w_B(t-\tau)\} \end{aligned} \quad (A1)$$

Using the assumption that signal and noise are uncorrelated, Equation (A1) simplifies using Equations (4) and (14)

$$\begin{aligned} R_{E,c,1}(\tau) &= \phi^2 \alpha_1^2 \bar{R}_y(\tau) R_{w_B}(\tau) \\ &= 2f_c N_0 \phi^2 \alpha_1^2 \text{tri}_{1/f_c}(\tau) R_{w_B}(\tau) \text{sinc}(2\pi f_c \tau) \\ &= (N_0)^2 (C/N_0)_1 (2f_c \phi^2) \text{sinc}(2\pi f_c \tau) \end{aligned} \quad (A2)$$

where the last step uses Equation (8).

APPENDIX B

TABULATED NUMERICAL RESULTS

The following tables provide numerical results to provide more accurate values than can be inferred from the plots in the earlier section. Where applicable, the analytical results are computed using numerical evaluation of the spectral dot products and thus may slightly differ from results computed using the approximate numerical values in Table 2. Table B1 lists results for codeless processing.

Tables B2, B3, and B4 list results for semicodeless processing, for different values of N .

Tables B5, B6, and B7 list results for soft-decision semicodeless processing, for different values of N .

TABLE B1 Numerical results for dual-channel codeless processing

$(C/N_0)_1$, dB-Hz	$(C/N_0)_2$, dB-Hz	Bilinear Approximation to $(C/N_0)_c$, dB-Hz	$(C/N_0)_c$, dB-Hz
41.5	38.5	12.7	12.7
44.0	41.0	17.7	17.7
46.5	43.5	22.7	22.7
49.0	46.0	27.7	27.6
51.5	48.5	32.7	32.6
54.0	51.0	37.7	37.5
56.5	53.5	42.7	42.3
59.0	56.0	47.7	47.0
61.5	58.5	52.7	51.5
40.0	40.0	12.7	12.7
42.5	42.5	17.7	17.7
45.0	45.0	22.7	22.7
47.5	47.5	27.7	27.7
50.0	50.0	32.7	32.6
52.5	52.5	37.7	37.5
55.0	55.0	42.7	42.4
57.5	57.5	47.7	47.1

(Continues)

TABLE B1 (Continued)

$(C/N_0)_1$, dB-Hz	$(C/N_0)_2$, dB-Hz	Bilinear Approximation to $(C/N_0)_c$, dB-Hz	$(C/N_0)_c$, dB-Hz
60.0	60.0	52.7	51.7
38.5	41.5	12.7	12.7
41.0	44.0	17.7	17.7
43.5	46.5	22.7	22.7
46.0	49.0	27.7	27.7
48.5	51.5	32.7	32.6
51.0	54.0	37.7	37.5
53.5	56.5	42.7	42.4
56.0	59.0	47.7	47.1
58.5	61.5	52.7	51.7

TABLE B2 Numerical results for dual-channel semicodeless processing, $N = 10$

$(C/N_0)_1$, dB-Hz	$(C/N_0)_2$, dB-Hz	Bilinear Approximation to $(C/N_0)_s$, dB-Hz	$(C/N_0)_s$, dB-Hz
41.5	38.5	19.2	19.1
44.0	41.0	24.2	24.1
46.5	43.5	29.2	28.9
49.0	46.0	34.2	33.8
51.5	48.5	39.2	38.5
54.0	51.0	44.2	43.0
56.5	53.5	49.2	47.2
59.0	56.0	54.2	51.1
61.5	58.5	59.2	54.7
40.0	40.0	19.2	19.1
42.5	42.5	24.2	24.1
45.0	45.0	29.2	29.0
47.5	47.5	34.2	33.8
50.0	50.0	39.2	38.5
52.5	52.5	44.2	43.0
55.0	55.0	49.2	47.3
57.5	57.5	54.2	51.3
60.0	60.0	59.2	54.9
38.5	41.5	19.2	19.1
41.0	44.0	24.2	24.1
43.5	46.5	29.2	28.9
46.0	49.0	34.2	33.8
48.5	51.5	39.2	38.5
51.0	54.0	44.2	43.0
53.5	56.5	49.2	47.2
56.0	59.0	54.2	51.1
58.5	61.5	59.2	54.7

TABLE B3 Numerical results for dual-channel semicodeless processing, $N = 20$

$(C/N_0)_1$, dB-Hz	$(C/N_0)_2$, dB-Hz	Bilinear Approximation to $(C/N_0)_s$, dB-Hz	$(C/N_0)_s$, dB-Hz
41.5	38.5	22.2	22.0
44.0	41.0	27.2	26.9
46.5	43.5	32.2	31.7
49.0	46.0	37.2	36.4
51.5	48.5	42.2	40.9
54.0	51.0	47.2	45.0
56.5	53.5	52.2	48.9
59.0	56.0	57.2	52.4
61.5	58.5	62.2	55.5
40.0	40.0	22.2	22.1
42.5	42.5	27.2	26.9
45.0	45.0	32.2	31.8
47.5	47.5	37.2	36.4
50.0	50.0	42.2	40.9
52.5	52.5	47.2	45.1
55.0	55.0	52.2	49.0
57.5	57.5	57.2	52.5
60.0	60.0	62.2	55.7
38.5	41.5	22.2	22.0
41.0	44.0	27.2	26.9
43.5	46.5	32.2	31.7
46.0	49.0	37.2	36.4
48.5	51.5	42.2	40.9
51.0	54.0	47.2	45.0
53.5	56.5	52.2	48.9
56.0	59.0	57.2	52.4
58.5	61.5	62.2	55.5

TABLE B4 Numerical results for dual-channel semicodeless processing, $N = 40$

$(C/N_0)_1$, dB-Hz	$(C/N_0)_2$, dB-Hz	Bilinear Approximation to $(C/N_0)_s$, dB-Hz	$(C/N_0)_s$, dB-Hz
41.5	38.5	25.2	24.9
44.0	41.0	30.2	29.7
46.5	43.5	35.2	34.3
49.0	46.0	40.2	38.7
51.5	48.5	45.2	42.8
54.0	51.0	50.2	46.6
56.5	53.5	55.2	50.0
59.0	56.0	60.2	53.2
61.5	58.5	65.2	56.0
40.0	40.0	25.2	24.9
42.5	42.5	30.2	29.7
45.0	45.0	35.2	34.4
47.5	47.5	40.2	38.8
50.0	50.0	45.2	42.9
52.5	52.5	50.2	46.8
55.0	55.0	55.2	50.2
57.5	57.5	60.2	53.4
60.0	60.0	65.2	56.3
38.5	41.5	25.2	24.9
41.0	44.0	30.2	29.7
43.5	46.5	35.2	34.3
46.0	49.0	40.2	38.7
48.5	51.5	45.2	42.8
51.0	54.0	50.2	46.6
53.5	56.5	55.2	50.0
56.0	59.0	60.2	53.2
58.5	61.5	65.2	56.0

TABLE B5 Numerical results for dual-channel soft-decision semicodeless processing, $N = 10$

$(C/N_0)_1$, dB-Hz	$(C/N_0)_2$, dB-Hz	Bilinear Approximation to $(C/N_0)_d$, dB-Hz	$(C/N_0)_d$, dB-Hz
41.5	38.5	23.6	23.4
44.0	41.0	28.6	28.3
46.5	43.5	33.6	33.1
49.0	46.0	38.6	37.8
51.5	48.5	43.6	42.3
54.0	51.0	48.6	46.5
56.5	53.5	53.6	50.3
59.0	56.0	58.6	53.8
61.5	58.5	63.6	57.0
40.0	40.0	23.6	23.5
42.5	42.5	28.6	28.4
45.0	45.0	33.6	33.2
47.5	47.5	38.6	37.9
50.0	50.0	43.6	42.5
52.5	52.5	48.6	46.8
55.0	55.0	53.6	50.8
57.5	57.5	58.6	54.4
60.0	60.0	63.6	57.7
38.5	41.5	23.6	23.5
41.0	44.0	28.6	28.4
43.5	46.5	33.6	33.3
46.0	49.0	38.6	38.0
48.5	51.5	43.6	42.6
51.0	54.0	48.6	46.9
53.5	56.5	53.6	51.0
56.0	59.0	58.6	54.7
58.5	61.5	63.6	58.0

TABLE B6 Numerical results for dual-channel soft-decision semicodeless processing, $N = 20$

$(C/N_0)_1$, dB-Hz	$(C/N_0)_2$, dB-Hz	Bilinear Approximation to $(C/N_0)_d$, dB-Hz	$(C/N_0)_d$, dB-Hz
41.5	38.5	26.6	26.3
44.0	41.0	31.6	31.1
46.5	43.5	36.6	35.7
49.0	46.0	41.6	40.1
51.5	48.5	46.6	44.3
54.0	51.0	51.6	48.0
56.5	53.5	56.6	51.5
59.0	56.0	61.6	54.6
61.5	58.5	66.6	57.5
40.0	40.0	26.6	26.3
42.5	42.5	31.6	31.2
45.0	45.0	36.6	35.9
47.5	47.5	41.6	40.4
50.0	50.0	46.6	44.6
52.5	52.5	51.6	48.5
55.0	55.0	56.6	52.1
57.5	57.5	61.6	55.3
60.0	60.0	66.6	58.3
38.5	41.5	26.6	26.4
41.0	44.0	31.6	31.2
43.5	46.5	36.6	35.9
46.0	49.0	41.6	40.5
48.5	51.5	46.6	44.8
51.0	54.0	51.6	48.8
53.5	56.5	56.6	52.4
56.0	59.0	61.6	55.7
58.5	61.5	66.6	58.7

TABLE B7 Numerical results for dual-channel soft-decision semicodeless processing, $N = 40$

$(C/N_0)_1$, dB-Hz	$(C/N_0)_2$, dB-Hz	Bilinear Approximation to $(C/N_0)_d$, dB-Hz	$(C/N_0)_d$, dB-Hz
41.5	38.5	29.6	29.0
44.0	41.0	34.6	33.6
46.5	43.5	39.6	38.0
49.0	46.0	44.6	42.0
51.5	48.5	49.6	45.8
54.0	51.0	54.6	49.1
56.5	53.5	59.6	52.2
59.0	56.0	64.6	55.1
61.5	58.5	69.6	57.8
40.0	40.0	29.6	29.1
42.5	42.5	34.6	33.8
45.0	45.0	39.6	38.2
47.5	47.5	44.6	42.4
50.0	50.0	49.6	46.3
52.5	52.5	54.6	49.7
55.0	55.0	59.6	52.9
57.5	57.5	64.6	55.8
60.0	60.0	69.6	58.6
38.5	41.5	29.6	29.2
41.0	44.0	34.6	33.8
43.5	46.5	39.6	38.4
46.0	49.0	44.6	42.6
48.5	51.5	49.6	46.5
51.0	54.0	54.6	50.1
53.5	56.5	59.6	53.3
56.0	59.0	64.6	56.3
58.5	61.5	69.6	59.0